

Resonance Effects from Substituents on L-Type Ligands Mediate Synthetic Control of Gold Nanocluster Frontier Orbital Energies

Hanna Morales Hernández,[#] Satoshi Ohtsuka,[#] Arshad Mehmood,[#] Wangshu Wen,[#] Jake Bordenca, Benjamin G. Levine, and Christopher J. Johnson*



Cite This: *J. Phys. Chem. Lett.* 2024, 15, 10244–10251



Read Online

ACCESS |

Metrics & More

Article Recommendations

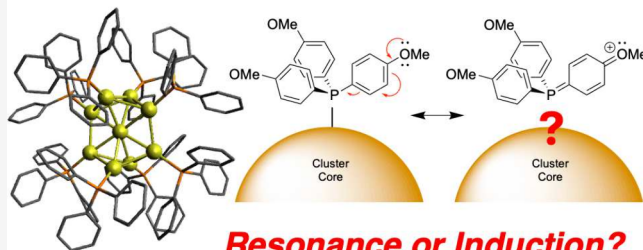
Supporting Information

ABSTRACT: The ligands of metal nanoclusters can be used to control their properties and reactivity, but a framework guiding their use remains elusive. Hammett studies of $\text{Au}_8(\text{PPh}_3)_7^{+}$ and $\text{Au}_9(\text{PPh}_3)_8^{3+}$ nanoclusters with *para*- and *meta*-methyl and -methoxy groups indicate that resonance effects, not inductive effects, yield quantitative shifts of the HOMO–LUMO transitions involving orbitals local to the cluster core. Individual ligand exchanges reveal that these shifts are caused by only four of seven ligands, inconsistent with inductive effects. Quantum chemical calculations predict no trend in Au atom charges with respect to Hammett parameter but do predict bond length trends expected for a resonance structure that includes the Au atoms. Computed orbitals show contributions from specific *para*-OMe oxygen lone pairs to the HOMO, indicating delocalization from the core to specific ligands. These results suggest that resonance structures could be drawn including Au and ligands, guiding efforts to modulate nanocluster electronic structure and energy transfer.

Atomically precise nanoclusters promise many of the desirable features of both nanoparticles and molecules. They typically have large absorption coefficients from the near-infrared to the ultraviolet,¹ a large but finite electronic density of states,² small redox potentials,³ and tunability through changes in size, structure, doping, and ligands.⁴ At the same time, it is sometimes possible to purify them with exact compositional specificity, and thus exact synthetic control of their properties and behaviors is conceivable using traditional chemical approaches. Their amenability to purification also allows their structures to be determined exactly using crystallography, revealing nanoscale structure–function relationships.⁵ This has led to a wide range of studies proposing nanoclusters as “designer” nanoparticles in contexts varying from biological sensing to catalysis.

The tunability of nanocluster size, structure, and composition yields three approaches to optimizing their properties in discrete steps for a given task. The smallest step in size is a difference of a single atom, but more typically, specific numbers of atoms are geometrically and electronically stable,^{6,7} and thus it is difficult to isolate clusters resulting from the stepwise addition or exchange of single atoms.⁸ Similarly, for a given number of atoms, only one or a few structures are typically known.⁹ Tuning by doping¹⁰ or by ligand exchange¹¹ can allow the fine-grained optimization of nanocluster properties, but can also make the purification of the resulting synthetic mixture much more challenging.¹²

Ligand Control of HOMO-LUMO Gap



Resonance or Induction?

Fine-tuning of molecules and coordination complexes is often achieved by chemical derivatization. As a result, well-developed frameworks exist for predicting how ligand derivatives affect electronic structure and properties of molecules and coordination complexes via bonding,¹³ electron withdrawing and donating effects,¹⁴ and steric effects,¹⁵ for example. Such a framework does not yet exist for nanoclusters, hampering the ability to rationally harness ligand chemistry to optimize nanocluster properties.

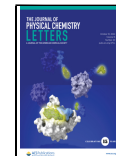
Nanoclusters formed from gold and phosphine ligands were among the first to be isolated and characterized crystallographically.¹⁶ In contrast to X-type thiolate ligands, L-type phosphine ligands could be expected to strongly electronically couple to the cluster core and thus to exert more influence over the electronic properties of the cluster. For instance, substitution of a single PPh_3 ligand by an N-heterocyclic carbene ligand has been shown to significantly enhance the galvanic efficiency of catalytic Au_{11} clusters.¹⁷ Mingos reported the crystal structures and spectra of a series of derivatives of $\text{Au}_9(\text{PPh}_3)_8^{3+}$ featuring -Me or -OMe substituents in the *para*

Received: September 3, 2024

Revised: September 27, 2024

Accepted: October 1, 2024

Published: October 2, 2024



positions of the PPh_3 ligands which showed that substitution induced marked changes in the electronic spectra of the clusters, but these changes were masked by gross structural rearrangement induced by the ligands in the solid state.^{16,18} The $\text{Au}_9(\text{PPh}_3)_8^{3+}$ and closely related $\text{Au}_8(\text{PPh}_3)_7^{2+}$ nanoclusters have been extensively investigated using quantum chemical,^{19–21} structural,^{22,23} spectroscopic,^{20,24} and mass spectrometric^{25–27} techniques. Crystal structures show that both clusters are oblate, though $\text{Au}_9(\text{PPh}_3)_8^{3+}$ can take on two different interchanging structural isomers in crystal structures in the presence of different counterions.^{23,28} Both clusters are best described within the superatomic model as 6-electron superatoms, having filled 1S , 1P_x (HOMO–1), and 1P_y (HOMO) orbitals.^{19,20} Despite not featuring a full 8-electron superatomic shell, their oblate structures are consistent with a geometric stabilization of the 1P_x and 1P_y and destabilization of the 1P_z orbitals such that they feature a large HOMO–LUMO gap. The destabilization of the 1P_z orbital is so significant that the apparent LUMO is actually the $1\text{D}_{x^2-y^2}$ superatomic orbital rather than 1P_z as would be expected.

We previously showed that the optical HOMO–LUMO gap of $\text{Au}_8(\text{PPh}_3)_7^{2+}$ and $\text{Au}_9(\text{PPh}_3)_8^{3+}$ could be systematically shifted by varying the substituent in *para*- position of the PPh_3 ligands, and that the magnitude of this shift was strongly correlated to the electron donating strength of substituent as measured by the Hammett *para* parameter σ_p .²⁹ Furthermore, the shift was apparently magnified by the higher charge of $\text{Au}_9(\text{PPh}_3)_8^{3+}$, which we hypothesized to indicate its higher electron withdrawing potential. Subsequent quantum chemical studies broadly reproduced the directions of these trends, but suggested a complex picture.²¹

These studies provided no insight into the underlying chemical principles mediating this control, however. The Hammett equation describes a linear free energy relationship that is defined in the context of the acidity of the carboxylic acid group of benzoic acid,¹⁴ but it has been observed to correlate to a number of commonly encountered chemical observables. The Hammett parameter is interpreted as a measure of electron withdrawing strength (for positive values) and is defined for both *para* (σ_p) and *meta* (σ_m) positions relative to the carboxylic acid group. The electron withdrawing or donating effect can be decomposed into inductive (σ_i) and resonance (σ_r) contributions, such that $\sigma_p \approx \sigma_i + \sigma_r$ and $\sigma_m \approx \sigma_r$, where *meta* substituents lack a resonance component since no probable resonance structure exists for this configuration. Thus, comparing *para*- and *meta*-substituted species makes it possible to determine whether inductive or resonance effects are responsible for an observed linear trend—if no trend holds for the *meta*-substituted clusters, the effect must be driven by resonance. These parameters are tabulated in Table S2.

Figure 1a presents the low-energy region of the spectra of all *meta*-substituted clusters studied here. In the case of $\text{Au}_8(\text{PPh}_3)_7^{2+}$, $\text{Au}_8(\text{P}(m\text{-CH}_3\text{-Ph})_3)_7^{2+}$, and $\text{Au}_8(\text{P}(m\text{-OCH}_3\text{-Ph})_3)_7^{2+}$, the HOMO–LUMO transition is easily identified for all three clusters at roughly 2.1 eV. The spectra are decomposed into individual contributions by fitting to a series of Gaussian functions to quantify the transition energies, yielding the dashed curves in Figure 1a. For $\text{Au}_9(\text{PPh}_3)_8^{3+}$, $\text{Au}_9(\text{P}(m\text{-CH}_3\text{-Ph})_3)_8^{3+}$, and $\text{Au}_9(\text{P}(m\text{-OCH}_3\text{-Ph})_3)_8^{3+}$, identification of the HOMO–LUMO transition is more challenging as it is significantly weaker, likely due to the higher symmetry of the cluster. $\text{Au}_9(\text{PPh}_3)_8^{3+}$ and $\text{Au}_9(\text{P}(m\text{-CH}_3\text{-Ph})_3)_8^{3+}$ both feature a single weak transition between 2.0 and 2.1 eV, while

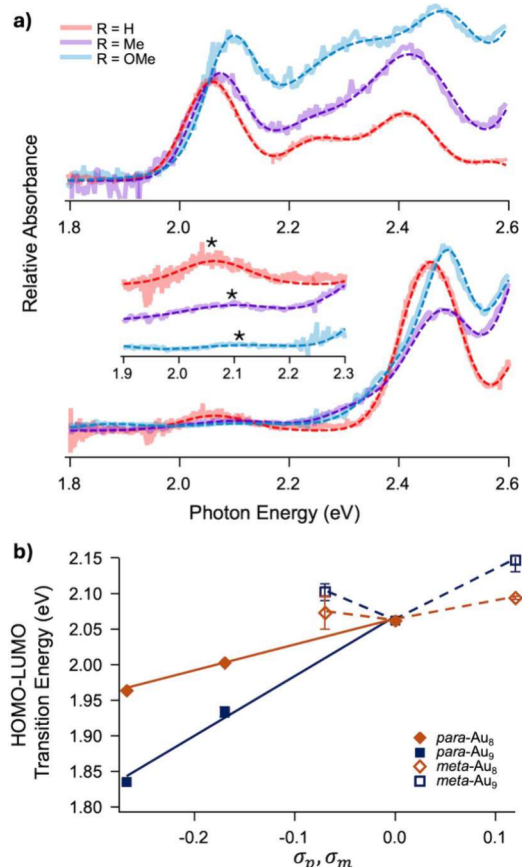


Figure 1. (a) An overview of the spectra of the *meta*-substituted clusters (solid), with corresponding fits to Gaussian absorption features (dashed). Top: the derivatives of $\text{Au}_8(\text{PPh}_3)_7^{2+}$. Bottom: the derivatives of $\text{Au}_9(\text{PPh}_3)_8^{3+}$. Inset: a detailed view of the weak apparent HOMO–LUMO transitions (* denotes the absorption max). (b) A plot of the HOMO–LUMO transition energies of *para* (filled markers)- or *meta* (open markers)-substituted clusters vs Hammett σ_p or σ_m , respectively, for $\text{Au}_8(\text{PPh}_3)_7^{2+}$ and $\text{Au}_9(\text{PPh}_3)_8^{3+}$ derivatives. Solid lines are linear fits for *para*-substituted clusters, dashed lines highlight the lack of a linear trend for *meta*-substituted clusters, and error bars are 1σ uncertainties in the fit values. For *para*-substituted clusters, errors bars are smaller than the markers.

$\text{Au}_9(\text{P}(m\text{-OCH}_3\text{-Ph})_3)_8^{3+}$ shows two features below 2.2 eV, one at 2.1 eV and one near 1.9 eV. We hypothesized that the lower energy peak was the result of a second isomer, induced by steric hindrance of the bulkier *meta*- $\text{P}(\text{Ph}-\text{OMe})_3$ ligands. This isomerization has been seen in *para*- $\text{P}(\text{Ph}-\text{OMe})_3$ -protected Au_9 clusters,²³ though we have not observed this spectroscopically.²⁹ We confirmed this hypothesis using two-laser double resonance experiments, as outlined in the Supporting Information, and thus disregard the 1.9 eV peak for this analysis. We note that, even if the true HOMO–LUMO transition energy were the 1.9 eV peak, the data would still significantly deviate from the trend for *para*-substituted clusters, and thus the conclusions of this work would still be supported.

These results immediately rule out simple steric-effect-induced isomerization as the cause for these shifts. Both *para*- and *meta*-substituted PPh_3 ligands are bulkier than PPh_3 , yet for both Au_8 and Au_9 , *para*-substituted clusters only show red shifts of the HOMO–LUMO transition while *meta*-substituted clusters only show blue shifts. Therefore, no trend with

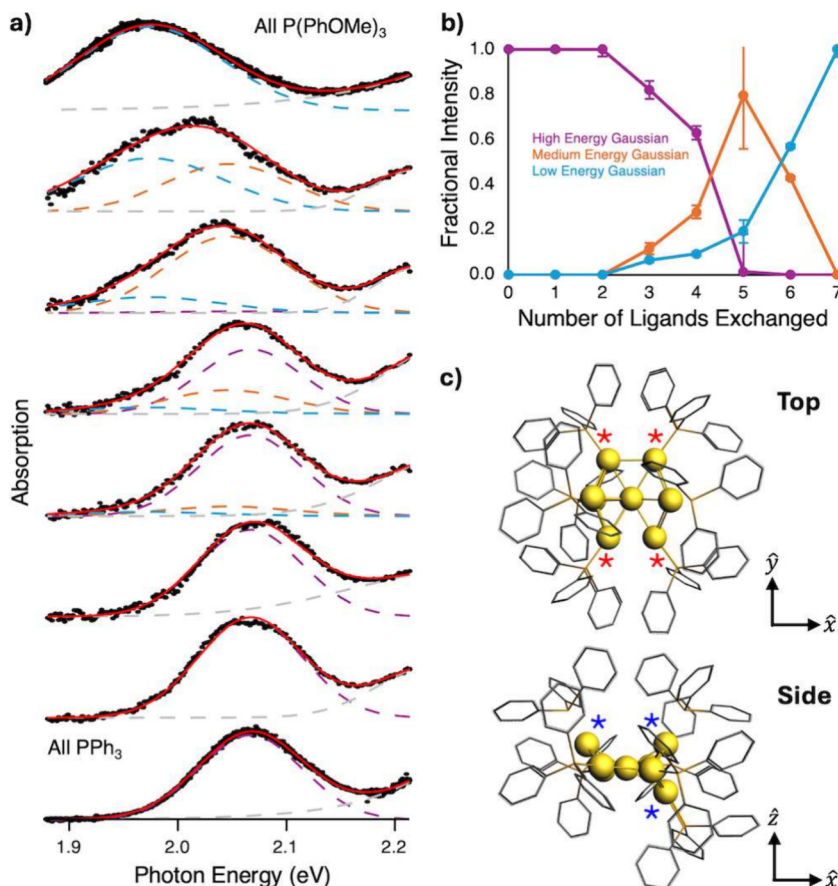


Figure 2. (a) Evolution of the HOMO–LUMO transition for sequentially *para*-exchanged clusters, with the fully exchanged cluster spectrum at top. Also shown by colored dashed lines are the peaks resulting from the constrained decomposition procedure described in the text, where purple is the lower energy peak, orange is the intermediate energy peak, and blue is the high energy peak. (b) A plot of the fractional contribution of each peak to the total experimental signal for each exchange. (c) Structures for $\text{Au}_8(\text{PPh}_3)_7^{2+}$ viewed from the top and side, with red * highlighting the ligand binding sites that we propose to be causing the shift, and blue * highlighting those that make no difference.

increased steric hindrance in the ligand shell is observed, and we must look to other factors to explain the spectral shifts.

Figure 1b plots the HOMO–LUMO transition energies of all *para*- and *meta*-substituted clusters against the corresponding Hammett parameters. It is immediately clear that the strong correlation found for *para*-substituted clusters is not reproduced for *meta*-substituted clusters. Indeed, the transition energies of the *meta*-substituted clusters do not even vary monotonically with respect to σ_m , and what variance they do display is substantially smaller than that of the *para*-substituted clusters. As is the case with the *para*-substituted clusters, the *meta*-substituted $\text{Au}_8(\text{PPh}_3)_7^{2+}$ clusters show a smaller magnitude of shift than the $\text{Au}_9(\text{PPh}_3)_8^{3+}$ clusters do, reinforcing the role of the charge of the cluster core in amplifying the ligand effect.

The absence of a trend for *meta*-substituted clusters indicates that resonance effects are responsible for the observed control of the HOMO–LUMO energy. Interestingly, resonance effects upon protonation have also been suggested to perturb ethynyl-protected Au_8 clusters by directly modulating π -conjugation through the ethynyl group.³⁰ However, the degree to which the putative resonance effect includes the Au atoms remains an open question. We consider two scenarios: a) that resonance includes both ligand substituent orbitals and core-local superatomic orbitals, or b) that resonance modulates the charge on the phosphorus atom,

which then inductively perturbs the superatomic orbitals. If resonance includes the cluster core, then we expect that the HOMO and LUMO form more probable resonance structures with some ligands than others, which will be observable as nonmonotonic shifts as a function of number of ligands exchanged. In other words, some ligands will contribute much more substantially than others to the total shift. If inductive effects at the phosphorus atoms are responsible for the shifts, we would expect more monotonic behavior, as electrostatic effects are additive to a reasonable approximation. To test this hypothesis, we recorded the individual spectrum of each partially *para*-OMe substituted $\text{Au}_8(\text{PPh}_3)_7^{2+}$. We chose $\text{Au}_8(\text{PPh}_3)_7^{2+}$ because the HOMO–LUMO transition of $\text{Au}_9(\text{PPh}_3)_8^{3+}$ is quite weak, and mixed ligands distribute the signal over a number of species. Mass selection of a specific mixture of ligands ensured that spectra for clusters with an exact number of ligands exchanged could be recorded unambiguously.

The spectra for sequentially substituted clusters show that most of the observed HOMO–LUMO red shift is driven by only four ligands, supporting the resonance hypothesis. Figure 2a shows the spectra upon sequential exchange of *para*-OMe substituted ligands. The spectra for 0–4 ligands exchanged are visually quite similar, while significant shifts are seen for 5–7 ligands exchanged. Only very small shifts of the peak centers are observed in the first four exchanges—a small even–odd

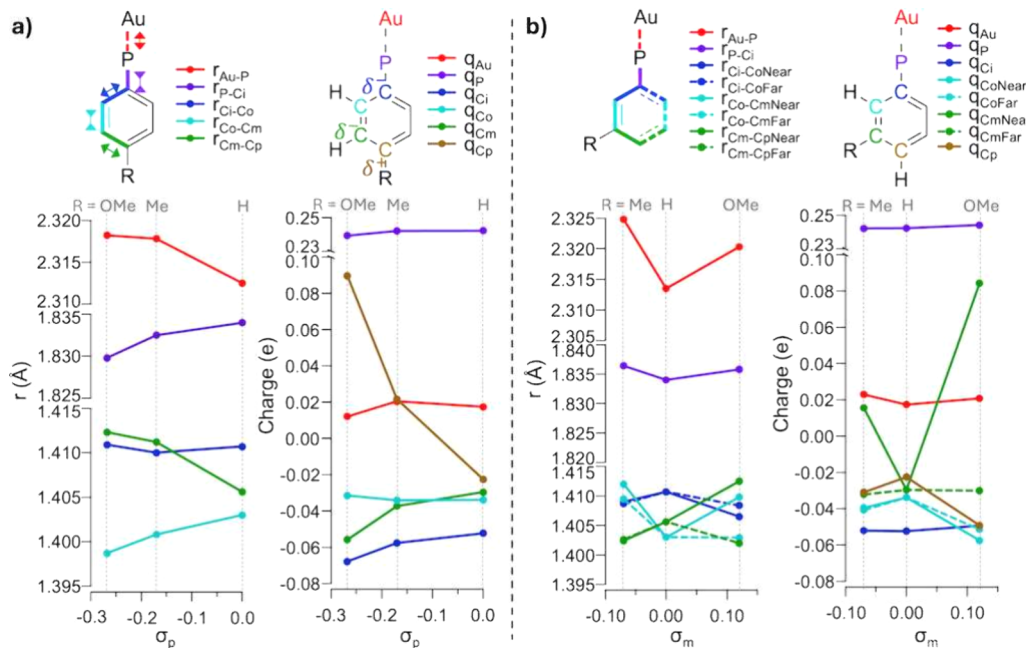


Figure 3. (a) The average bond lengths (left) and atomic charges (right) as computed by BP86+D3/cc-pVQZ-pp for the fully *para*-substituted $\text{Au}_8(\text{PPh}_3)_7^{2+}$ clusters with respect to the Hammett *para* parameter (σ_p). In both cases, quantities are averaged over all chemically equivalent bonds/atoms in the $\text{Au}_8(\text{PPh}_3)_7^{2+}$ system. At the top is an explanation of the color coding of the figures along with the expected trends as the *para* substituent changes from H to Me to OMe, assuming resonance is the dominant effect. C_i is the *ipso* carbon with respect to the P atom, C_o is the *ortho* carbon, C_m is the *meta* carbon, and C_p is the *para* carbon. (b) The same, but for fully *meta*-substituted clusters.

sequence of blue and red shifts appears to be present, but its amplitude is only around 5% of the total magnitude of the shift. After the fifth exchange, a clear trend emerges in the peak position, with each subsequent exchange contributing approximately equal energy shifts to the HOMO–LUMO transition. It is not clear from the experiment in which order specific ligand sites are exchanged, though we can hypothesize that the first three exchanged ligands are bound to Au atoms above and below the 5-Au quasi-plane (blue * in Figure 2c). The HOMO and LUMO superatomic orbitals are expected to predominantly lie in the quasi-plane, increasing their overlap with the ligands at these sites (red * in Figure 2c).

The shapes of the HOMO–LUMO peaks can all be explained by decomposing them into three Gaussian contributions: one that matches that of $\text{Au}_8(\text{PPh}_3)_7^{2+}$, one that matches that of $\text{Au}_8(\text{P}(p\text{-OCH}_3\text{-Ph})_3)_7^{2+}$, and one that represents an intermediate peak or set of peaks. We perform this decomposition using a maximally constrained approach by first fitting the unsubstituted and fully substituted spectra separately to obtain peak centers and widths, as shown in Figure 2a. We then fit the spectrum for $\text{Au}_8(\text{PPh}_3)_2(\text{P}(p\text{-OCH}_3\text{-Ph})_3)_5^{2+}$ to three Gaussian functions, two with the exact peak positions and widths of the unsubstituted and fully substituted peaks (varying only their amplitudes) and an intermediate peak for which all parameters were varied. Finally, all other spectra were fitted to these three Gaussian functions, with their positions and widths fixed and only their amplitudes allowed to vary. This procedure minimized the risk of overfitting while allowing the evolution of the HOMO–LUMO band to be quantitatively tracked. The plausibility of this approach is supported by the fact that the width of the presumed intermediate energy peak is midway between the widths of the unexchanged and fully exchanged peaks. While this approach is sufficient to fully decompose the spectra, we

emphasize that it by no means suggests that only one transition or cluster composition is responsible for the intermediate peak. We chose to use this procedure rather than simply fitting the bands and tracking the shifts for two reasons: first, the band shapes for partially exchanged clusters were not well fit by single Gaussian functions, particularly due to an apparent low energy shoulder that appeared in the spectra for the clusters after three and four substitutions, and second, because we have no reason to assume that each partially exchanged cluster features only one combination of exchanged and unexchanged ligand sites, making it likely that several different exchange isomers exist for any given number of exchanges.

The evolution of the relative contributions of the three components of the HOMO–LUMO peak (Figure 2b) supports our observation that some ligands affect the energy of the transition. It is clear that the first two exchanges have no effect whatsoever on the composition of the peak, and that the third and fourth exchanges play only a minor role. Looking specifically at the formation of the higher energy component associated with the fully exchanged cluster, 80% of its amplitude is recovered only in the last two ligand exchanges. The simplest explanation for this observation is that certain ligands play essentially no role in determining the HOMO–LUMO transition energy, while other ligands play a large role, and the latter are preferentially exchanged last likely due to their increased binding affinity driven by their resonance interactions with the core. Given that the HOMO (superatomic P_x) and LUMO (superatomic $D_{x^2-y^2}$) both lie in the five-atom plane of the core, we expect that these sites, highlighted with red asterisks in Figure 2c, are the exchange sites driving the shift. Thus, we conclude that resonance-driven inductive effects from the ligand P atoms to the core can not explain these results.

Given that charges and bond lengths are not directly observable in our experiments, we turned to quantum chemical methods to gain further insight. We again focus on $\text{Au}_8(\text{PPh}_3)_7^{2+}$ because there is no uncertainty as to the isomeric structure of this cluster. To probe whether the resonance effects extend into the gold core, we analyzed the computed bond lengths and atomic charges for the fully substituted clusters. Without extensive conformational sampling of the rotatable ligand bonds, it is not possible to reproduce the energetic trend with respect to Hammett parameter, but these more local properties can be more robustly described by computing a single conformation. Resonance electron donating effects at the *para*- position will tend to increase the quinoidal character of the PPh_3 ligand, leading to a shortening of the $\text{C}_{meta}-\text{C}_{ortho}$ and P–C bond lengths and elongation of the other two aromatic C–C bonds, as shown in the scheme on the top left of Figure 3a. If resonance extends to the cluster core, then we expect a lengthening of the Au–P bond with decreasing σ_p . On the left side of Figure 3a is a summary of the computed bond lengths of $\text{Au}_8(\text{PPh}_3)_7^{2+}$ with each *para* substituent. We do indeed find the expected alternating pattern of shorter and longer bonds that increases in magnitude with decreasing σ_p of the *para* substituent. Notably, the increase in the Au–P bond length is approximately the same as the increase of the $\text{C}_{para}-\text{C}_{meta}$ bond, indicating that the resonance effect has not decayed despite relaying through five bonds. A version of these plots with respect to σ_r is given in Figure S1.

The trends in computed atomic charges are also more consistent with a resonance effect than an inductive effect. Assuming a resonance effect, we expect to see specific trends with decreasing σ_p : increasing charge at the *para*-carbon and decreasing charge at the *meta*- and *ipso*-carbons. In the case of an inductive effect, we would expect the sign of the charge changes to be the same, and to decay for each atom further away from the *para*-carbon. Indeed, we observe the former trend in the computed atomic charges, shown on the right side of Figure 3. We also see a small and monotonic decrease of the charge on the P atom with decreasing σ_p , but we do not see a monotonic change of the charge on the adjacent Au atoms. Since an inductive effect on the Au atom should be most directly driven by the adjacent P atom charge, this further argues against inductive effects driving the changes in charges in this cluster.

Applying the same analysis to the computed charges for *meta*-substituted $\text{Au}_8(\text{PPh}_3)_7^{2+}$ as depicted in Figure 3a, we again see that the charges on the P atoms vary monotonically with inductive electron donation as measured by σ_m , but the charges on the Au atoms do not. Indeed, the bond lengths and charges for the *meta*-substituted clusters generally do not vary monotonically. Thus, the observed trend in the HOMO–LUMO transition energies can not be explained by an inductive effect from the P atoms, regardless of whether or not resonance effects are significant within the ligands.

The observation of clear resonance effects is perhaps somewhat surprising because, while the HOMO and LUMO of $\text{Au}_8(\text{PPh}_3)_7^{2+}$ and $\text{Au}_9(\text{PPh}_3)_8^{3+}$ are superatomic orbitals delocalized across the cluster core, this result suggests that there is still some clear contribution to those orbitals from Au–ligand bonding that should be able to be rationalized in a manner similar to that of a mononuclear coordination complex. We consider two possibilities: that there is a relatively local bonding orbital at the Au–P interface that

mixes with the cluster core-based HOMO and/or LUMO superatomic orbitals, or that the HOMO and/or LUMO superatomic orbitals are more extensively delocalized onto the ligands. The fact that the ground state bond lengths and charges show evidence of resonance effects indicates that one of these cases must hold for the HOMO. However, it is unclear if either applies to the LUMO.

To determine the degree of delocalization, we performed time-dependent density functional theory calculations of the HOMO–LUMO transition. Indeed, extensive delocalization is observed. Figure 4a presents the HOMO as approximated by the hole of a natural transition orbital for *para*- and *meta*-OMe

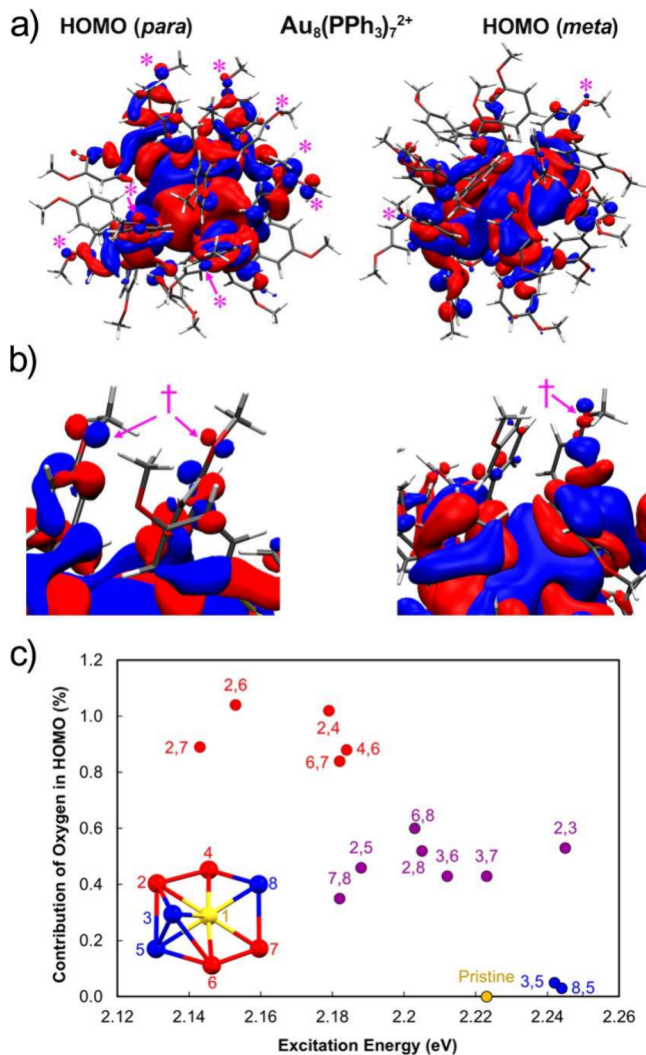


Figure 4. (a) Depictions of the HOMO orbitals for $\text{Au}_8(\text{PPh}_3)_7^{2+}$ substituted with OMe in the *para* and *meta* positions, as determined for an isosurface value of 0.005. Contributions from oxygen atomic orbitals are highlighted by*. (b) Images focusing on example oxygen orbital shapes for these orbitals, noted with †, that demonstrate the out of plane nature of the oxygen *p* orbital in the *para*- case and the in plane nature in the *meta*- case. These orbitals were computed via natural transition orbital analysis.³¹ (c) Each data point represents one $\text{Au}_8(\text{PPh}_3)_7^{2+}$ cluster doubly substituted by ligands with OMe at the *para* position. The possible substitution sites are subdivided into two groups (red and blue) in the inset. Clusters with zero, one, or two substitutions at the red sites are indicated by blue, purple, and red data points, respectively. For reference, pristine (unsubstituted) $\text{Au}_8(\text{PPh}_3)_7^{2+}$ is shown as a yellow point.

substituted $\text{Au}_8(\text{PPh}_3)_7^{2+}$, where * highlights OMe oxygen atomic orbital contributions for clarity. Mulliken analysis indicates that the fraction of the HOMO that sits on these oxygen atoms is ~ 7 times greater in the *para* versus *meta* case. Further, 38% of the HOMO resides on the ligand in the *para* case, compared to only 33% for *meta*. In contrast, only very modest *para/meta* effects are seen in the LUMO, shown in Figure S2. The large difference in the degree of delocalization in the *para*- versus *meta*- case is again consistent with the assignment of the shift in the HOMO–LUMO transition energy to resonance effects that reach into the Au core. This further indicates that the optical HOMO–LUMO gap shift seen in the experiment is driven by modulation of the hole energy in the excited state. Only some of the OMe groups contribute significantly to the delocalized cluster core orbitals, likely due to a complex interplay of symmetry effects.

To assess whether all ligand sites interact equivalently with the core, similar TDDFT calculations were performed on a series of $\text{Au}_8(\text{PPh}_3)_7^{2+}$ clusters with exactly two ligands substituted by OMe at the *para* positions. As seen in Figure 4c, some sites couple more strongly to the HOMO–LUMO excitation than others. If both substitutions occur at the in-plane sites colored red in the inset, approximately one percent of the HOMO population is found to reside on the OMe oxygen atoms, and a red shift of 0.03–0.08 eV is observed in the vertical excitation energy. In contrast, when both substitutions occur at an out-of-plane blue site (atoms 3, 5, and 8), almost no HOMO population is observed on the OMe oxygen atoms, and a 0.02 eV blue shift is observed in the excitation energy. Therefore, substitution at the red sites couples much more strongly to the HOMO–LUMO transition than those at blue sites. Clusters in which one substitution occurs each at a red and blue site (purple dots in Figure 4c) exhibit intermediate behavior, suggesting that the effect of sequential substitution at the red sites is roughly additive. Analysis of the Kohn–Sham orbital energies supports the assertion that delocalization of the HOMO onto the ligands drives the dependence of the HOMO–LUMO transition energy on position of substitution (Figures S3 and S4).

The results of Figure 4c thus support our hypothesis that the minimal change of the HOMO–LUMO transition upon the first several substitutions is due to preferential substitution at the out-of-plane sites 3, 5, and 8, while the significant red shifts for the last four are due to substitution at the in-plane sites 2, 4, 6, and 7. Intermediate shifts can be explained either by substitution and a mixture of these sites. We therefore tentatively assign the lowest energy feature from the fitting procedure discussed above to be resulting from primarily substitution at in-plane sites, and the intermediate feature to partial substitution at both groups of sites.

Taken together, these results suggest that the intuitive framework developed to rationalize ground and excited state resonance in molecules and coordination complexes likely still holds for nanoclusters, at least up to 8–9 Au atoms. Attempts to extend this detailed framework to nanoclusters requires a merging of the delocalized superatomic model of the cluster core with the atomistic picture of bonding. Such a framework will be invaluable to facilitate the deliberate engineering of optimized nanoclusters for various applications. Furthermore, the observation of explicit resonance effects extending from the cluster core superatomic orbitals to substituents on the periphery of the ligand shell supports the use of the ligand–environment interface as an active participant in energy and

charge transfer processes between the cluster core and the environment. Engineering the ligand–environment interface is thus likely to be an important step in the optimization of nanocluster properties and performance.

EXPERIMENTAL SECTION

The clusters studied here were synthesized using an approach that has been previously reported,²⁹ with specific details described in the Supporting Information.

We recorded the electronic absorption spectra of these clusters using a mass spectrometry-based technique that alleviates the need for purification of the as-synthesized reaction mixture—the mass spectrometer is effectively the separation device. The combination of exact selectivity, minimal environmental effects, and low temperature of this experiment yields highly reproducible, well resolved spectra of unambiguously purified nanoclusters. All experiments were conducted on a home-built ion trap time-of-flight (TOF) mass spectrometer. The experimental process has been explained in detail previously.³² Briefly, the clusters are introduced into the instrument using electrospray ionization (ESI) of solutions of ~ 1 mg/mL in methanol. Upon storage in a cryogenically cooled octopole ion trap containing helium, the ions are collisionally cooled to near the trap temperature (3.6–3.8 K), at which point tens of He atoms (referred to as “tags”) adsorb onto the clusters. A pulsed optical parametric oscillator, spanning the region 409–719 nm, intersects the tagged clusters in the cryogenic trap, 10 μs prior to their extraction. Absorption of a photon resonant with the cluster’s electronic transitions results in desorption of all tags, yielding an untagged peak in the mass spectrum. The integrated intensities of the tagged and untagged clusters are recorded as a function of wavelength, and a linear absorption spectrum is generated from the ratio of the latter to the total cluster signal after correcting for the laser power spectrum.

Cluster structures were generated via geometry optimization of reported crystal structures at the BP86+D3^{33–35}/cc-pVDZ-pp^{36,37} level. Time-dependent density functional theory calculations were performed using the CAM-B3LYP+D3^{35,38}/cc-pVDZ-pp functional to avoid well-known charge delocalization errors. Hirschfeld and Mulliken populations and orbital composition analyses were performed using the MultiWFN package.³⁹ All calculations were performed in the ORCA 5.0.3 software package.⁴⁰

ASSOCIATED CONTENT

Supporting Information

The Supporting Information is available free of charge at <https://pubs.acs.org/doi/10.1021/acs.jpcllett.4c02580>.

Synthetic and experimental procedures, discussion of isomer study, tabulated Hammett parameters, plots of bond lengths and charges with respect to σ , and additional orbital images (PDF)

AUTHOR INFORMATION

Corresponding Author

Christopher J. Johnson — Department of Chemistry, Stony Brook University, Stony Brook, New York 11794, United States;  orcid.org/0000-0003-1859-5615; Phone: (631) 632-7577; Email: chris.johnson@stonybrook.edu

Authors

Hanna Morales Hernández – Department of Chemistry, Stony Brook University, Stony Brook, New York 11794, United States; orcid.org/0009-0000-7113-0150

Satoshi Ohtsuka – Department of Chemistry, Stony Brook University, Stony Brook, New York 11794, United States; Institute for Advanced Computational Science, Stony Brook University, Stony Brook, New York 11794, United States

Arshad Mehmood – Division of Information Technology - Research Computing, Informatics & Innovation and Institute for Advanced Computational Science, Stony Brook University, Stony Brook, New York 11794, United States; orcid.org/0000-0001-7819-3648

Wangshu Wen – Department of Chemistry, Stony Brook University, Stony Brook, New York 11794, United States

Jake Bordenca – Department of Chemistry, Stony Brook University, Stony Brook, New York 11794, United States; orcid.org/0009-0004-4651-1911

Benjamin G. Levine – Department of Chemistry, Stony Brook University, Stony Brook, New York 11794, United States; Institute for Advanced Computational Science, Stony Brook University, Stony Brook, New York 11794, United States; orcid.org/0000-0002-0356-0738

Complete contact information is available at:

<https://pubs.acs.org/10.1021/acs.jpcllett.4c02580>

Author Contributions

#H.M.H., S.O., A.M., and W.W. contributed equally to this work.

Notes

The authors declare no competing financial interest.

ACKNOWLEDGMENTS

H.M.H., J.B., W.W., and C.J.J. acknowledge support from the United States Department of Energy under grant number DE-SC0021991 and from the Air Force Office of Scientific Research under grant number FA9550-19-1-0105. S.O., A.M., and B.G.L. gratefully acknowledge support from the U.S. Department of Energy, Office of Science, Office of Basic Energy Sciences, under Award No. DE-SC0021643 and from the Institute for Advanced Computational Science.

REFERENCES

- (1) Jin, R. Atomically precise metal nanoclusters: stable sizes and optical properties. *Nanoscale* **2015**, *7*, 1549–1565.
- (2) Walter, M.; Akola, J.; Lopez-Acevedo, O.; Jadzinsky, P. D.; Calero, G.; Ackerson, C. J.; Whetten, R. L.; Grönbeck, H.; Häkkinen, H. A unified view of ligand-protected gold clusters as superatom complexes. *P. Natl. Acad. Sci. USA* **2008**, *105*, 9157–9162.
- (3) Kwak, K.; Lee, D. Electrochemistry of Atomically Precise Metal Nanoclusters. *Acc. Chem. Res.* **2019**, *52*, 12–22.
- (4) Jin, R.; Li, G.; Sharma, S.; Li, Y.; Du, X. Toward Active-Site Tailoring in Heterogeneous Catalysis by Atomically Precise Metal Nanoclusters with Crystallographic Structures. *Chem. Rev.* **2021**, *121*, 567–648.
- (5) Jadzinsky, P. D.; Calero, G.; Ackerson, C. J.; Bushnell, D. A.; Kornberg, R. D. Structure of a Thiol Monolayer-Protected Gold Nanoparticle at 1.1 Å Resolution. *Science* **2007**, *318*, 430–433.
- (6) Knight, W. D.; Clemenger, K.; de Heer, W. A.; Saunders, W. A.; Chou, M. Y.; Cohen, M. L. Electronic Shell Structure and Abundances of Sodium Clusters. *Phys. Rev. Lett.* **1984**, *52*, 2141–2143.
- (7) Reber, A. C.; Khanna, S. N. Superatoms: Electronic and Geometric Effects on Reactivity. *Acc. Chem. Res.* **2017**, *50*, 255–263.
- (8) Kang, X.; Li, Y.; Zhu, M.; Jin, R. Atomically precise alloy nanoclusters: syntheses, structures, and properties. *Chem. Soc. Rev.* **2020**, *49*, 6443–6514.
- (9) Xu, W. W.; Zeng, X. C.; Gao, Y. The structural isomerism in gold nanoclusters. *Nanoscale* **2018**, *10*, 9476–9483.
- (10) Takano, S.; Tsukuda, T. Chemically Modified Gold/Silver Superatoms as Artificial Elements at Nanoscale: Design Principles and Synthesis Challenges. *J. Am. Chem. Soc.* **2021**, *143*, 1683–1698.
- (11) Wang, Y.; Bürgi, T. Ligand exchange reactions on thiolate-protected gold nanoclusters. *Nanoscale Adv.* **2021**, *3*, 2710–2727.
- (12) Niihori, Y.; Koyama, Y.; Watanabe, S.; Hashimoto, S.; Hossain, S.; Nair, L. V.; Kumar, B.; Kurashige, W.; Negishi, Y. Atomic and Isomeric Separation of Thiolate-Protected Alloy Clusters. *J. Phys. Chem. Lett.* **2018**, *9*, 4930–4934.
- (13) Griffith, J. S.; Orgel, L. E. Ligand-field theory. *Q. Rev. Chem. Soc.* **1957**, *11*, 381–393.
- (14) Hammett, L. P. The Effect of Structure upon the Reactions of Organic Compounds. Benzene Derivatives. *J. Am. Chem. Soc.* **1937**, *59*, 96–103.
- (15) Tolman, C. A. Steric effects of phosphorus ligands in organometallic chemistry and homogeneous catalysis. *Chem. Rev.* **1977**, *77*, 313–348.
- (16) Mingos, D. M. P.; Lewis, J.; Green, M. L. H. Some theoretical and structural aspects of gold cluster chemistry. *Philos. Trans. R. Soc. S-A* **1982**, *308*, 75–83.
- (17) Narouz, M. R.; Osten, K. M.; Unsworth, P. J.; Man, R. W. Y.; Salorinne, K.; Takano, S.; Tomihara, R.; Kaappa, S.; Malola, S.; Dinh, C.-T.; et al. N-heterocyclic carbene-functionalized magic-number gold nanoclusters. *Nat. Chem.* **2019**, *11*, 419–425.
- (18) Hall, K. P.; Theoblad, B. R. C.; Gilmour, D. I.; Mingos, D. M. P.; Welch, A. J. Synthesis and structural characterization of $[Au_9\{P(p-C_6H_4OMe)\}_{38}]^{\pm}$ cluster with a centred crown of gold atoms. *J. Chem. Soc., Chem. Commun.* **1982**, *528*–530.
- (19) Karimova, N. V.; Aikens, C. M. Time Dependent Density Functional Theory Study of Magnetic Circular Dichroism Spectra of Gold Clusters $Au_9(PH_3)_8^{3+}$ and $Au_9(PPPh_3)_8^{3+}$. *J. Phys. Chem. A* **2016**, *120*, 9625–9635.
- (20) Fagan, J. W.; Weerawardene, K. L. D. M.; Cirri, A.; Aikens, C. M.; Johnson, C. J. Toward quantitative electronic structure in small gold nanoclusters. *J. Chem. Phys.* **2021**, *155*, 014301.
- (21) Day, P. N.; Pachter, R.; Nguyen, K. A. Calculated linear and nonlinear optical absorption spectra of phosphine-ligated gold clusters. *Phys. Chem. Chem. Phys.* **2022**, *24*, 11234–11248.
- (22) van der Velden, J. W. A.; Bour, J. J.; Bosman, W. P.; Noordik, J. H. Synthesis and X-ray crystal structure determination of the cationic gold cluster compound $[Au_8(PPPh_3)_7](NO_3)_2$. *J. Chem. Soc., Chem. Commun.* **1981**, *1218*–1219.
- (23) Briant, C. E.; Hall, K. P.; Mingos, D. M. P. Structural characterisation of two crystalline modifications of $[Au_9P(C_6H_4OMe)_3]_{38}^{3-}$: the first example of skeletal isomerism in metal cluster chemistry. *J. Chem. Soc., Chem. Commun.* **1984**, *290*–291.
- (24) Madridejos, J. M. L.; Harada, T.; Falcinella, A. J.; Small, T. D.; Golovko, V. B.; Andersson, G. G.; Metha, G. F.; Kee, T. W. Optical Properties of the Atomically Precise C_4 Core $[Au_9(PPPh_3)_8]^{3+}$ Cluster Probed by Transient Absorption Spectroscopy and Time-Dependent Density Functional Theory. *J. Phys. Chem. C* **2021**, *125*, 2033–2044.
- (25) Hirata, K.; Chakraborty, P.; Nag, A.; Takano, S.; Koyasu, K.; Pradeep, T.; Tsukuda, T. Interconversions of Structural Isomers of $[PdAu_8(PPPh_3)_8]^{2+}$ and $[Au_9(PPPh_3)_8]^{3+}$ Revealed by Ion Mobility Mass Spectrometry. *J. Phys. Chem. C* **2018**, *122*, 23123–23128.
- (26) Hewitt, M. A.; Hernández, H.; Johnson, G. E. ESI-MS Identification of the Cationic Phosphine-Ligated Gold Clusters Au_{1-22} : Insight into the Gold–Ligand Ratio and Abundance of Larger Clusters. *J. Am. Soc. Mass Spectrom.* **2021**, *32*, 237–246.
- (27) Muramatsu, S.; Nakahigashi, Y.; Omoda, T.; Takano, S.; Tsukuda, T.; Inokuchi, Y. Collision-Induced Fission of Oblate Gold Superatom in $[Au_9(PPPh_3)_8]^{3+}$: Deformation-Mediated Mechanism. *J. Phys. Chem. Lett.* **2023**, *14*, 5641–5647.

- (28) Wen, F.; Englert, U.; Gutrath, B.; Simon, U. Crystal Structure, Electrochemical and Optical Properties of $[\text{Au}_9(\text{PPh}_3)_8](\text{NO}_3)_3$. *Eur. J. Inorg. Chem.* **2008**, *2008*, 106–111.
- (29) Cirri, A.; Morales Hernández, H.; Kmiotek, C.; Johnson, C. J. Systematically Tuning the Electronic Structure of Gold Nanoclusters through Ligand Derivatization. *Angew. Chem., Int. Ed.* **2019**, *58*, 13818–13822.
- (30) Kobayashi, N.; Kamei, Y.; Shichibu, Y.; Konishi, K. Protonation-Induced Chromism of Pyridylethynyl-Appended [core +exo]-Type Au_8 Clusters. Resonance-Coupled Electronic Perturbation through π -Conjugated Group. *J. Am. Chem. Soc.* **2013**, *135*, 16078–16081.
- (31) Martin, R. L. Natural transition orbitals. *J. Chem. Phys.* **2003**, *118*, 4775–4777.
- (32) Cirri, A.; Hernández, H. M.; Johnson, C. J. High Precision Electronic Spectroscopy of Ligand-Protected Gold Nanoclusters: Effects of Composition, Environment, and Ligand Chemistry. *J. Phys. Chem. A* **2020**, *124*, 1467–1479.
- (33) Becke, A. D. Density-functional Exchange-energy Approximation with Correct Asymptotic Behavior. *Phys. Rev. A* **1988**, *38*, 3098–3100.
- (34) Perdew, J. P. Density-functional Approximation for the Correlation Energy of the Inhomogeneous Electron Gas. *Phys. Rev. B* **1986**, *33*, 8822–8824.
- (35) Grimme, S.; Ehrlich, S.; Goerigk, L. Effect of the damping function in dispersion corrected density functional theory. *J. Comput. Chem.* **2011**, *32*, 1456–1465.
- (36) Wilson, A. K.; Woon, D. E.; Peterson, K. A.; Dunning, T. H. Gaussian basis sets for use in correlated molecular calculations. IX. The atoms gallium through krypton. *J. Chem. Phys.* **1999**, *110*, 7667–7676.
- (37) Metz, B.; Stoll, H.; Dolg, M. Small-core multiconfiguration-Dirac–Hartree–Fock-adjusted pseudopotentials for post-d main group elements: Application to PbH and PbO. *J. Chem. Phys.* **2000**, *113*, 2563–2569.
- (38) Yanai, T.; Tew, D. P.; Handy, N. C. A new Hybrid Exchange–correlation Functional Using the Coulomb-attenuating Method (CAM-B3LYP). *Chem. Phys. Lett.* **2004**, *393*, 51–57.
- (39) Lu, T.; Chen, F. Multiwfn: A Multifunctional Wavefunction Analyzer. *J. Comput. Chem.* **2012**, *33*, 580–592.
- (40) Neese, F.; Wennmohs, F.; Becker, U.; Ripplinger, C. The ORCA quantum chemistry program package. *J. Chem. Phys.* **2020**, *152*, 224108.